Effective models for CO_2 migration in geological systems with varying topography

Sarah E. Gasda[1], Halvor M. Nilsen[2], Helge K. Dahle[3], and William G. Gray[4]

H. K. Dahle, Department of Mathematics, University of Bergen, Johannes Brunsgate 12, 5020 Bergen, Norway. (Helge.Dahle@math.uib.no)

S. E. Gasda, Center for Integrated Petroleum Research, Uni Research, Allégaten 41, 5020 Bergen, Norway. (Sarah.Gasda@uni.no)

W. G. Gray, Department of Environmental Sciences and Engineering, University of North Carolina at Chapel Hill, 148 Rosenau Hall, Chapel Hill, NC 27599-7431 USA. (WGGray@unc.edu)

H. M. Nilsen, Applied Mathematics, SINTEF, Forskningsveien 1, 0314 Oslo, Norway. (Halvor-Moll.Nilsen@sintef.no)

[1]Center for Integrated Petroleum

Abstract. Geological CO_2 sequestration relies on a competent sealing layer, or caprock, that bounds the formation top and prevents vertical migration of CO_2 and brine. Modeling studies have shown that caprock topography, or roughness, can significantly decrease updip migration speed of CO_2 and increase structural trapping. Caprock roughness can be characterized at different spatial scales. For instance, regional-scale features such as domes, traps, and spill points can be detected in seismic surveys and have been shown to affect large-scale migration patterns. However, structural and topographical variability, known as rugosity, exists below seismic detection limits but can be measured at the scale of centimeters and meters using LiDAR scanning of formation outcrops. Little is known about the actual impact of structural rugosity on CO_2 plume migration.

Research, Uni Research, Bergen, Norway.

[2]Applied Mathematics, SINTEF, Oslo, Norway.

[3]Department of Mathematics, University of Bergen, Bergen, Norway.

[4]Department of Environmental Sciences and Engineering, University of North Carolina at Chapel Hill, Chapel Hill, North Carolina, USA.

Practically speaking, given the large scales required to model commercial scale CO_2 storage projects and the limitations on computational power, only seismic-scale caprock topography can be resolved using standard discretization techniques. Therefore, caprock variability that exists below the model resolution scale is defined as subscale and must be handled by upscaling. In this paper, we derive effective equations for CO_2 migration that include the impact of fine-scale variability in caprock topography using static equilibrium upscaling, an approach that is adapted for the vertical equilibrium modeling framework. The effective equations give estimates of the impact of rugosity on CO_2 plume migration and trapping in large-scale systems.

1. Introduction

Geological carbon storage involves injection of large quantities of CO_2 into the deep subsurface and relies upon various trapping mechanisms to stabilize the injected CO_2 and prevent unwanted migration over long timescales. Because CO_2 is less dense and much less viscous than the resident brine under typical storage conditions, it rises to the top of the injection formation and forms a thin layer of mobile, high-saturation CO_2 underneath a low-permeability sealing unit, or caprock. Structural and topographical variability of this upper boundary can affect migration and long-term trapping of CO_2 in the subsurface [*Ambrose et al.*, 2008]. This impact is clearly evident in seismic surveys of the CO_2 plume migration in the Utsira Sand, Norway [*Hermanrud et al.*, 2009] and has been examined for realistic geological models [*Nilsen et al.*, 2012] and idealized surface structures [*Gray et al.*, 2012]. Structural heterogeneity affects CO_2 plume migration direction and speed [*Gray et al.*, 2012], thus influencing the evolution of the CO_2 footprint over time.

The caprock boundary is most often not a smooth flat surface, but has natural variability that spans several length scales. For instance, at the basin scale of hundreds of kilometers, geological structure is controlled by regional uplift and other paleogeological mechanisms and can be characterized by a dip angle that may be approximately constant for a given basin [*Ambrose et al.*, 2008]. The dip angle can be estimated from geological basin maps and databases [*Alberta Geological Survey*, 2011]. At the reservoir scale of tens of kilometers, the topography is more varied; and structures such as domes, anticlines and traps can be identified in the caprock surface. These features, which we refer to collectively as *roughness*, can be observed from seismic surveys with a resolution of

approximately 10 m [*Jackson et al.*, 2010]. Below this scale, the variability in surface topography is referred to as *rugosity* and is characterized as sub-meter fluctuations of the interface between the permeable formation and the relatively impermeable caprock. This variability is impossible to detect from seismic measurements but may be inferred from observations of outcrops (LiDAR scanning) and geostatistical earth models [*Pringle et al.*, 2010; *Jones et al.*, 2009]. For instance, recent LiDAR scans of outcrops in North America have detected rugosity at the scale of tens of centimeters for scans that span tens of kilometers [*Bellian et al.*, 2005]. These high-resolution datasets have unprecedented potential to increase our understanding of CO_2 migration in real systems.

Due to the potential importance of topography, reliable numerical models are needed that can capture the impact of large- and small-scale roughness on CO_2 migration. In practice, because CO_2 storage sites may be on the order of tens to hundreds of kilometers in extent [*Celia and Nordbotten*, 2009; *Nordbotten and Celia*, 2012], resolution of fine-scale caprock roughness using standard grid resolution techniques is computationally prohibitive. One alternative approach is to assume vertical equilibrium (VE) of pressure, which allows for partial integration of the multiphase flow equations and leads to the well-known VE model [*Dietz*, 1953; *Coats et al.*, 1971; *Gasda et al.*, 2009; *Gray et al.*, 2012]. As demonstrated in [*Gray et al.*, 2012] and [*Nilsen et al.*, 2010], the VE model captures CO_2 migration along variable caprock topography more reliably and efficiently compared to a standard full-dimensional simulator for systems in which the assumptions of vertical equilibrium and gravity segregation are valid. The VE model is ultimately more accurate because the model formulation (vertical integration combined with gravity segregation) essentially leads to infinite vertical resolution of the CO_2 plume, eliminat-

ing the vertical discretization issues inherent in a full-dimensional model [*Nilsen et al.*, 2010]. The efficiency is improved for the VE model by solving two-dimensional, instead of three-dimensional, equations thereby immensely reducing the size of the computational problem. In addition, the VE model eliminates the timestep restrictions introduced by the vertical resolution and makes the pressure-transport coupling weaker, further increasing computational efficiency [*Ingeborg and Nilsen*, 2010].

Despite the efficiency of VE models, it is not possible to resolve all relevant structural features in large domains that may cover hundreds to thousands of square kilometers. In these situations, VE models can resolve regional scale topography at the scale of hundreds of meters, however, caprock rugosity requires some form of upscaling. To this end, we develop an effective model to capture the impact of subscale caprock roughness on CO_2 migration by horizontally upscaling the depth-integrated variables that appear in the VE modeling framework. Specifically, we derive effective permeability and relative permeability functions for fine-scale caprock roughness using analytical and numerical homogenization techniques. Depth-integrated permeability (or transmissibility) is upscaled based on the homogeneous-equation approaches used for a periodic medium [*Renard and de Marsily*, 1997]. The depth-integrated relative permeability functions are upscaled using a quasi-steady state approach assuming a fixed fine-scale saturation, which is analogous to employing the capillary equilibrium assumption for a heterogeneous medium [*Pickup and Stephen*, 2000; *Neuweiler and Vogel*, 2007].

Subsequently, we demonstrate the model concept for cross-sectional systems that are simple enough to be upscaled analytically. We then apply the upscaling approach to caprock surfaces with complex variation in topography. Finally, we discuss how the effec-

tive model can be applied to real geological systems, which will be the subject of future work.

2. System Description

Our objective is to derive an effective model for the system depicted in Figure 1 that consists of a reservoir with top and bottom boundaries whose vertical locations are described by functions $\zeta_T(x, y)$ and $\zeta_B(x, y)$, respectively. Within this aquifer, two mobile fluid phases exist, CO_2 (c) and brine (b), along with associated residual phases. A certain number of simplifying assumptions are made for this system. For instance, the rock and fluid phases are modeled as incompressible. We also assume that the fluid phases are completely segregated by gravity and vertical fluid pressure is at equilibrium. This implies that at any given horizontal location, the fluid phases are vertically distributed according to density; and the vertical flow component for each phase is negligible. In addition, we assume that capillary forces are negligible such that a sharp-interface assumption can be applied to this system. This assumption implies uniform saturations in each fluid phase rather than a resolved capillary fringe, a condition which is still compatible with the upscaling approach used later that invokes the capillary equilibrium assumption. Within the context of VE models, the equilibrium assumption is applied to the location of the sharp interface rather than the fine-scale capillary pressure. More details on this approach are provided later.

The assumptions described above provide three macroscopic regions, created by CO_2 displacing the brine by a drainage process and re-imbibition of brine where the CO_2 front has receded, which are ordered in a well-defined way. The bottommost region contains mobile brine at 100% saturation. The residual CO_2 region, containing mobile brine with

residual CO_2 following imbibition, is bounded below by $\zeta_R(x, y, t)$. The topmost region consists of mobile CO_2 phase with residual brine that was trapped during the drainage process. The bottom boundary of of this region is represented by $\zeta_M(x, y, t)$.

The interfaces are ordered such that $\zeta_B \leq \zeta_R \leq \zeta_M \leq \zeta_T$. The vertical dimension of each region is described by the thickness $h_i,\ i = c, r, b$, where $h_c = \zeta_T - \zeta_M$, $h_r = \zeta_M - \zeta_R$, $h_b = \zeta_R - \zeta_B$, and $\sum_i h_i = H(x, y)$. Due to the sharp-interface assumption, the local CO_2 saturation s_c is uniform within each region and defined as follows,

$$s_c = \begin{cases} 0, & \text{if} \quad \zeta_B \leq z < \zeta_R \\ s_{cr}, & \text{if} \quad \zeta_R \leq z < \zeta_M \\ 1 - s_{br}, & \text{if} \quad \zeta_M \leq z \leq \zeta_T. \end{cases} \tag{1}$$

where, $s_{\alpha r}$ are the residual saturations of phase $\alpha = c, b$.

Next, we will describe our approach to upscaling rugosity effects within the VE modeling framework. We derive effective permeability and relative permeability functions that upscale both the migration retardation and enhanced trapping of CO_2 due to subscale topographical features. First, we describe a simple conceptualization of the effective model using permeability arguments, which we call the *accretion layer* model. This model is useful for gaining insight into CO_2 migration and trapping in a rough caprock system. It also provides the foundation for a set of consistent effective functions derived using steady-state homogenization techniques. The latter approach is based on the assumption of static capillary equilibrium applied to a system of interest when upscaling the flow equations and deriving the effective functional forms for permeability and relative permeability in two-dimensional and three-dimensional systems.

3. VE Model

A VE model is used in combination with horizontal upscaling to derive effective equations for subscale caprock roughness. The VE model is therefore defined as the "fine-scale" model used for comparison with the horizontally averaged, i.e. "coarse-scale", models. Here, the fine-scale is the depth-integrated scale consisting of vertically integrated variables and equations. The VE model derivation from three-dimensional, REV-scale equations is described in this section. However in previous work, the VE model has been derived from the micro-scale directly to the depth-integrated scale [*Gray et al.*, 2012].

The VE model formulation is based upon vertical integration of the three-dimensional flow equations (REV scale) under the assumption that the fluids are in vertical equilibrium (i.e. vertical flow can be neglected) and the fluids are completely segregated due to gravity [*Lake*, 1989]. The VE assumption is reasonable for CO_2 sequestration systems because of large aspect ratios of typical storage systems (many kilometers in lateral extent compared with tens to hundreds of meters in reservoir thickness) [*Yortsos*, 1995]. In addition, strong buoyancy forces (density contrast $\Delta\rho$ on the order of 200 to 400 kg/m^3) lead to rapid gravity segregation. These dominant physical characteristics result in equilibrium of the vertical pressure profile over relatively short timescales. The VE model has been employed historically for strongly segregated flows in petroleum reservoirs [*Dietz*, 1953; *Coats et al.*, 1971; *Lake*, 1989; *Huppert and Woods*, 1995] and more recently for CO_2 sequestration in saline aquifers [*Nordbotten and Celia*, 2006; *Neufeld and Huppert*, 2009; *Hesse et al.*, 2008; *Gasda et al.*, 2011; *Nordbotten and Celia*, 2012].

The VE model can include several processes relevant for CO_2 storage, such as a local capillary transition zone [*Nordbotten and Dahle*, 2011] or convection-driven dissolution [*Gasda et al.*, 2011], that are implemented as subgrid components within the overall

framework. However, the objective of this study is to investigate the effect of the caprock structure. Therefore, we neglect mass transfer and capillarity and assume a sharp interface between the two fluid phases. This further simplifies the integrated equations and subsequent analysis.

To begin, we consider the three-dimensional mass conservation equations for CO_2 and brine phases in an incompressible system,

$$\frac{\partial}{\partial t}(\phi s_\alpha) + \nabla \cdot \mathbf{u}_\alpha = q_\alpha, \quad \alpha = c, b. \tag{2}$$

In the above equation, ϕ is porosity, s_α is the phase saturation, $\mathbf{u}_\alpha$ is the volumetric phase flux, and q_α is the volumetric source/sink term per unit volume. Here, $\mathbf{u}_\alpha$ is given by Darcy's law [*Bear*, 1972],

$$\mathbf{u}_\alpha = -\frac{k_\alpha \mathbf{k}}{\mu_\alpha} \cdot (\nabla p_\alpha - \rho_\alpha \mathbf{g}) \tag{3}$$

where $\mathbf{k}$ is the permeability tensor, k_α is the phase relative permeability, μ_α is the phase viscosity, p_α is the phase pressure, ρ_α is the phase density, and $\mathbf{g}$ is the gravitational vector.

The integration is performed between the bottom and top boundaries of the storage aquifer or reservoir, assuming impermeable shale layers bound the system above and below. The vertical direction (z) is defined as perpendicular to the local dipping plane of the reservoir, such that flow is predominantly in the lateral direction (x and y). The resulting two-dimensional equations consist of integrated variables such as thickness of mobile and residual CO_2 regions and depth-integrated horizontal phase fluxes. The details of the integration can be found in previous work, see [*Gasda et al.*, 2009, 2011; *Nordbotten and Celia*, 2012], and will not be repeated in detail here. A brief overview of the integrated 2D equations is given.

After integration of Equation (2), we obtain the lateral 2D conservation of mass equation for components CO_2 and brine with upscaled variables (capital letters indicate vertically upscaled),

$$\frac{\partial}{\partial t}\left(H\Phi S_\alpha\right) + \nabla_\parallel \cdot \mathbf{F}_{\parallel\alpha} = Q_\alpha, \quad \alpha = c, b. \tag{4}$$

In the integrated equation, Φ is depth-averaged porosity, S_α is the depth-integrated saturation, $H(x, y)$ is spatially varying aquifer thickness, defined as $H(x, y) = \zeta_T(x, y) - \zeta_B(x, y)$, Q_α is the depth-integrated source/sink term, $(\cdot)_\parallel$ represent lateral operators and quantities. Depth-integrated saturation is defined as

$$H\Phi S_\alpha = \int_{\zeta_B}^{\zeta_T} \phi s_\alpha \, \mathrm{d}z, \quad \alpha = c, b. \tag{5}$$

The mass fluxes $\mathbf{F}_{\parallel\alpha}$ are obtained by vertically integrating the lateral component of phase fluxes and gives the resulting upscaled flux expression,

$$\mathbf{F}_{\parallel\alpha} = \int_{\zeta_B}^{\zeta_T} \mathbf{u}_{\parallel\alpha} \, \mathrm{d}z, \quad \alpha = c, b. \tag{6}$$

After integration, assuming the lateral gradients in pressure are constant in the vertical dimension, the resulting depth-integrated flux expression is,

$$\mathbf{F}_{\parallel\alpha} = -\frac{H\mathbf{K}_{\parallel\alpha} \cdot \mathbf{K}_\parallel}{\mu_\alpha} \cdot \left(\nabla_\parallel p_\alpha - \rho_\alpha \mathbf{g}_\parallel\right), \quad \alpha = c, b. \tag{7}$$

where $\mathbf{K}_\parallel$ is the depth-integrated permeability tensor given by

$$H\mathbf{K}_\parallel = \int_{\zeta_B}^{\zeta_T} \mathbf{k}_\parallel \, \mathrm{d}z, \tag{8}$$

and $\mathbf{K}_{\parallel\alpha}$ is the depth-integrated relative permeability tensor of phase α given by,

$$H\mathbf{K}_{\parallel\alpha} \cdot \mathbf{K}_\parallel = \int_{\zeta_B}^{\zeta_T} \mathbf{k}_\parallel k_\alpha \, \mathrm{d}z, \quad \alpha = c, b. \tag{9}$$

For convenience, we will omit the $(\cdot)_\parallel$ notation from this point forward.

Since pressure is in vertical equilibrium based on the Dupuit approximation [*Lake*, 1989; *Gasda et al.*, 2011; *Nordbotten and Celia*, 2012], the phase pressure p_α in Equation (7) can be determined from a reference phase pressure P_α calculated at some datum level, $z = \zeta_P$. For the expressions that follow $\zeta_P = \zeta_B$. The reference phase pressures can be related by the location of the ζ_M interface and local capillary pressure. Since we have neglected local capillary pressure, then $P_n - P_b = \mathbf{e}_z \cdot \mathbf{g}\Delta\rho(\zeta_M - \zeta_B)$, where $\Delta\rho = \rho_b - \rho_c$. Using $P = P_b$ as the primary pressure variable we obtain the following local pressure distribution for each phase,

$$p_b = P + \mathbf{e}_z \cdot \mathbf{g}\rho_b \left(z - \zeta_B\right), \quad \text{for } \zeta_B \leq z \leq \zeta_M, \tag{10}$$

and

$$p_c = P + \mathbf{e}_z \cdot \mathbf{g}\left[\rho_b \left(\zeta_M - \zeta_B\right) + \rho_c \left(z - \zeta_M\right)\right], \quad \text{for } \zeta_M \leq z \leq \zeta_T. \tag{11}$$

We see that the pressure is not obtained for a phase where it is immobile. By substitution of Equations (10) and (11) into Equation (7) we have,

$$\mathbf{F}_b = -\frac{H\mathbf{K}_b \cdot \mathbf{K}}{\mu_b} \cdot \left[\nabla P - \nabla\left(\mathbf{e}_z \cdot \mathbf{g}\rho_b\zeta_B\right) - \rho_b\mathbf{g}\right], \tag{12}$$

and

$$\mathbf{F}_c = -\frac{H\mathbf{K}_c \cdot \mathbf{K}}{\mu_c} \cdot \left[\nabla P + \nabla\left(\mathbf{e}_z \cdot \mathbf{g}\Delta\rho\zeta_M\right) - \nabla\left(\mathbf{e}_z \cdot \mathbf{g}\rho_b\zeta_B\right) - \rho_c\mathbf{g}\right]. \tag{13}$$

Note that the z terms in expression Equations (10) and (11) disappear when taking the lateral gradient of p_α.

Together, Equations (4)–(13) represent the fine-scale system of equations consisting of depth-integrated variables. The VE model, which can be solved analytically under certain simplifying assumptions, must be solved numerically for heterogeneous systems (see [*Gray et al.*, 2012; *Gasda et al.*, 2012]). The fine-scale VE model must also resolve

the topographical heterogeneity of the caprock to correctly capture fluid flow in a rough caprock system.

For the purpose of later analysis, it is useful to have a fractional flow formulation of the VE model. By combining Equations (12) and (13) and defining the total flux as $\mathbf{F}_t = \mathbf{F}_b + \mathbf{F}_c$, we can obtain a fractional flow expression for CO_2 flux. Then, by substitution into Equation (4), we have,

$$\frac{\partial H\Phi S_c}{\partial t} + \nabla \cdot \left\{ \mathbf{\Lambda}_c \cdot \mathbf{\Lambda}_t^{-1} \cdot \mathbf{F}_t - H\mathbf{\Lambda}_c \cdot \mathbf{\Lambda}_b \cdot \mathbf{\Lambda}_t^{-1} \cdot \mathbf{K} \cdot \left[\nabla \left(\mathbf{e}_z \cdot \mathbf{g} \Delta\rho \zeta_M \right) + \Delta\rho \mathbf{g} \right] \right\} = Q_c, \quad (14)$$

where $\mathbf{\Lambda}_\alpha = \mathbf{K}_\alpha / \mu_\alpha$ are the upscaled mobility tensors for $\alpha = c, b$, and $\mathbf{\Lambda}_t = \mathbf{\Lambda}_b + \mathbf{\Lambda}_c$. This equation can be solved numerically, however analytical solutions can also be obtained under additional simplifying conditions, i.e. zero total and diffusive fluxes. This will be discussed further in the next section.

4. 1-D Effective Model

We derive coarse-scale equations for the system depicted in Figure 1 in one horizontal dimension, where the fine scale system is a 2-D vertical cross-section (x-z) with spatially varying top and bottom boundaries. First, we devise a simple effective model called the accretion-layer model (AM). This approach has the advantage that it can be solved analytically under simplifying conditions to gain insight into the behavior of CO_2 in rough caprock systems. This discussion is followed by more rigorous upscaling based on steady-state techniques to obtain a homogeneous-equation model (HM) for the cross-sectional system.

In both upscaling approaches, we define an averaging volume (inset in Figure 1) that has a length scale L much smaller than the overall length scale of the storage aquifer. This

allows us to resolve the large-scale topographical variation, while upscaling the subscale topography that may be too small to resolve in flow simulations. In the upscaling, we replace the varying topography with flat top and bottom boundaries. The result is an effective aquifer height, $\bar{H}$, which is defined as the horizontal average of the fine-scale thickness. In one dimension, this becomes

$$\bar{H} = \frac{1}{L}\int_0^L [\zeta_T(x) - \zeta_B(x)]\ \mathrm{d}x.$$

We also define a horizontally averaged brine thickness as,

$$\bar{h}_b = \frac{1}{L}\int_0^L [\zeta_M(x) - \zeta_B(x)]\ \mathrm{d}x.$$

and therefore $\bar{h}_c = \bar{H} - \bar{h}_b$ by definition. In regard to notation, we indicate horizontally upscaled coarse variables with an over-bar (e.g. $\bar{S}_\alpha$,$\bar{h}_\alpha$,...).

For the sake of brevity, we limit our presentation of the effective equations to drainage conditions ($h_r = 0$). This is appropriate because the most significant effect of topography on CO_2 migration occurs at the plume leading edge as brine is displaced by CO_2. However, the inclusion of imbibition is relatively straightforward and is incorporated into the final upscaled equations. We also assume spatially homogeneous fluid properties and a flat aquifer bottom, located at $z = \zeta_B(x) = 0$, for simplicity in both the AM and HM derivations. A flat aquifer bottom is reasonable given that variation in the bottom surface is less important for CO_2 migration than the top surface. Because we limit our derivation to one dimension, the two-dimensional tensorial quantities in the previous section become scalars.

4.1. Accretion-layer model

We assume that undulations in caprock topography create a volume within which CO_2 collects but otherwise cannot flow. At the average scale, we represent this trapped volume as an accretion layer, which is a constant thickness layer that has the equivalent volume as the trapped volume created by the variable topography. The thickness of this layer is determined from the specific topography being considered that varies in space at a length scale smaller than the averaged scale.

The right panel in Figure 2 depicts the effective system after horizontal upscaling. The dark-shaded accretion layer has a constant thickness A over the averaging length, such that the area of the accretion layer equals the area of the dark-shaded region of trapped CO_2 in the fine-scale system to the left. For convenience we define $a = A/\bar{H}$ and an effective aquifer thickness, $H_e = (1-a)\,\bar{H}$, which is the height of the aquifer through which CO_2 and brine can flow horizontally.

The key component of the AM conceptualization is the assumption that the accretion layer has zero horizontal permeability. This implies that while CO_2 and brine may flow in the lower regions, once CO_2 displaces brine from the accretion layer it remains structurally trapped regardless of additional accumulation of CO_2 below. The accretion layer can be interpreted as an instantaneous CO_2 sink.

The vertical distribution of horizontal permeability within this effective system is given as,

$$k(z) = \begin{cases} k, & \text{for } 0 \le z < H_e \\ 0, & \text{otherwise.} \end{cases} \tag{15}$$

We obtain the definition of coarse scale variables, such as permeability, relative permeability and saturation, by vertical integration over the effective aquifer thickness $\bar{H}$ according to the definitions in Section 3. For instance, applying Equations (1) and (5) to

this system gives the following average saturations,

$$\bar{H}\Phi\bar{S}_b = \phi\left(\bar{h}_c s_{br} + \bar{h}_b\right), \quad \bar{H}\Phi\bar{S}_c = \phi\bar{h}_c\left(1 - s_{br}\right). \tag{16}$$

The aquifer permeability given in Equation (15) can be integrated according to Equation (8),

$$\bar{H}\bar{K} = H_e k. \tag{17}$$

while depth-integrated relative permeability functions (Equation (9)) become,

$$\bar{H}\bar{K}_b\bar{K} = \begin{cases} \bar{h}_b k_b^0 k & \bar{h}_b \le H_e, \\ H_e k_b^0 k & H_e \le \bar{h}_b \le \bar{H}, \end{cases} \quad \bar{H}\bar{K}_c\bar{K} = \begin{cases} \left(H_e - \bar{h}_b\right) k_c^r k & \bar{h}_b \le H_e, \\ 0 & H_e \le \bar{h}_b \le \bar{H}, \end{cases} \tag{18}$$

where k_b^0 is the endpoint relative permeability of formation water, and k_c^r is the endpoint relative permeability of CO_2 during drainage. In pure saline aquifers $k_b^0 = 1$, while $k_b^0 < 1$ for reservoirs with residual hydrocarbons. In this derivation, the only mobile phases are CO_2 and brine.

At this point, we can combine the one-dimensional form of Equation (14) with Equations (16)–(18) and the definition of upscaled mobilities $\bar{\Lambda}_\alpha = \bar{K}_\alpha/\mu_\alpha$ to obtain the one-dimensional fractional flow equation for CO_2 in terms of brine thickness,

$$-\phi\left(1 - s_{br}\right)\frac{\partial\bar{h}_b}{\partial t} + \frac{\partial}{\partial x}\left[\frac{\bar{\Lambda}_c}{\bar{\Lambda}_t}\bar{F}_t + \frac{\bar{H}\bar{\Lambda}_c\bar{\Lambda}_b k\Delta\rho}{\bar{\Lambda}_t}\left(g\cos\theta\frac{\partial\bar{h}_b}{\partial x} + g\sin\theta\right)\right] = 0. \tag{19}$$

where θ is the tilt of the aquifer relative to the horizontal datum. Equation (19) describes three characteristic CO_2 fluxes for this system [*Huppert and Woods*, 1995; *Juanes et al.*, 2010; *Hesse et al.*, 2008]. The first term in the bracket expression contains a total flux $\bar{F}_t$ and describes CO_2 flux due to background fluid flow. The first part of the second term is dependent on the slope of the CO_2-brine interface, $\partial\bar{h}_b/\partial x$, and describes the parabolic or diffusive spreading of the CO_2 plume over time. The second part of this term gives the CO_2 flux along a sloping surface due to the buoyancy, which is a hyperbolic flux.

The relative importance of each characteristic flux has been examined previously using time scale arguments for limiting cases without background flow [*Hesse et al.*, 2008] and with background fluid flow [*Juanes et al.*, 2010; *MacMinn et al.*, 2010]. For instance, while the parabolic flux is more important at early time, this component dissipates quickly and for long-term migration we can assume that $\partial \bar{h}_b/\partial x$ is small compared to other terms. Also, in the neglecting background flux (i.e. $\bar{F}_t \approx 0$), we can omit the first term in the bracketed expression of Equation (19) in the following analysis. So, keeping only the hyperbolic component, we obtain

$$-\phi\,(1-s_{br})\,\frac{\partial \bar{h}_b}{\partial t} + \frac{\partial}{\partial x}\left[\frac{\bar{H}\bar{\Lambda}_c\bar{\Lambda}_b k\Delta\rho}{\bar{\Lambda}_t} g\sin\theta\right] = 0. \tag{20}$$

For analysis, it is convenient to define the following,

$$\frac{\bar{H}\bar{\Lambda}_c\bar{\Lambda}_b k\Delta\rho}{\bar{\Lambda}_t} g\sin\theta = \kappa\bar{\mathcal{F}}_b,$$

which can also be rearranged to the form

$$\left(\bar{H}\lambda_b^0 M k\Delta\rho g\sin\theta\right)\frac{\bar{\Lambda}_c\bar{\Lambda}_b}{\bar{\Lambda}_t\lambda_b^0 M} = \kappa\bar{\mathcal{F}}_b,$$

where the mobility ratio is $M = \lambda_c^r/\lambda_b^0$. In this form, it is easy to identify part of the group on the left as κ, which is the characteristic depth-integrated flux due to buoyancy along a sloped caprock surface. The other grouping is then $\bar{\mathcal{F}}_b$, which is the dimensionless flux function. Now, Equation (20) can be written more compactly as a classic hyperbolic equation,

$$-\phi(1-s_{br})\frac{\partial \bar{h}_b}{\partial t} + \frac{\partial\left(\kappa\bar{\mathcal{F}}_b\right)}{\partial x} = 0, \tag{21}$$

which can be treated analytically for insight into the behavior of CO_2 migration along a sloping rough caprock surface.

The first step is to obtain the the expression for $\bar{\mathcal{F}}_b$ by substitution of Equation (18) above into definitions of $\bar{\Lambda}_\alpha$ resulting in,

$$\bar{\mathcal{F}}_b = \begin{cases} \dfrac{1}{H_e} \dfrac{\bar{h}_b \left(H_e - \bar{h}_b\right)}{(1-M)\,\bar{h}_b + M H_e} & 0 \le \bar{h}_b \le H_e, \\ 0 & H_e \le \bar{h}_b \le \bar{H}. \end{cases} \tag{22}$$

This flux function has the same functional form in the effective layer ($0 \le h_b \le H_e$) as the forms analyzed in *Hesse et al.* [2008] and elsewhere, leading to rarefaction waves at the plume tip. However because of the accretion layer, $(H_e - \bar{H}) \le h_b \le \bar{H}$, the flux function defined by Equation (22) is non-convex, as seen in Figure 3a, and the tip of the plume will now develop a discontinuity (shock) according to hyperbolic analysis. We can analyze the shock using a line drawn tangent to the flux function curve from $\bar{h}_b/\bar{H} = 1$. By definition, the slope of the tangent line is equal to the derivative of the flux function ($\bar{\mathcal{F}}_b'$) at the tangent point (h_b^*). The tangent-line concept is shown graphically in Figure 3a, and mathematically can be written as,

$$\frac{\bar{\mathcal{F}}_b(h_b^*)}{1 - h_b^*} = -\bar{\mathcal{F}}_b'(h_b^*). \tag{23}$$

The solution to Equation (23) can be found analytically in this simple case (see [*Leveque*, 1990]). In brief, the analytical solution gives a dimensionless brine thickness at the shock tip,

$$h_b^* = \frac{M H_e}{H_e - (1-M)\bar{H}} \left(1 - \sqrt{\frac{\bar{H} - H_e}{M \bar{H}}}\right), \tag{24}$$

from which we can calculate the dimensionless CO_2 height at the shock tip $h_c^* = (1 - h_b^*)$ and convert to units of length by multiplication with $\bar{H}$. The analytical solution also gives the constant speed at which the CO_2 tip migrates upslope,

$$v_c^* = \frac{\kappa}{\phi(1 - s_{br})} \left(\frac{\bar{\mathcal{F}}_b(h_b^*)}{1 - h_b^*}\right), \tag{25}$$

which is simply a rescaling of the characteristic speed $\kappa/\phi(1-s_{br})$ by the slope of the tangent line. We note that this analysis is correct when other waves of the full solution do not interact with the hyperbolic wave at the tip. However, we gain important insight into the impact of caprock roughness from analysis of this special case.

There are several interesting observations obtained from this analysis. First, we note that in the limit as $a \to 0$, the thickness of CO_2 at the shock tip approaches zero. Thus, as $h_b^* \to 1$ the slope of the tangent line, $-\bar{\mathcal{F}}_b'(h_b^*)$, approaches unity. This implies that for flat sloping caprocks, the plume tip will have a reference speed equal to $v_0 = \kappa/\phi(1-s_{br})$, which is an expected result [*Hesse et al.*, 2008].

We also observe in Figure 3a that the tangent slope decreases with increasing a and M, resulting in slower tip velocities for caprock with higher amplitude roughness or more unfavorable mobility ratios. Figure 3b shows that the impact of a on tip speed compared with the reference velocity v_0 can be significant. In the case of a favorable displacement $M = 1$, the shock speed is 48% lower than v_0 for $a = 0.1$, while the impact is greater for larger mobility ratios. This implies that the presence of an accretion layer has a greater impact when the CO_2 plume is very thin at the leading edge, which occurs for increasingly unfavorable displacements.

4.2. Steady-state homogenization

In this section, we derive the effective medium functions for a rough caprock system by averaging the VE equations horizontally, which results in the HM approach. In doing so, we follow traditional homogenization techniques that have been developed for upscaling permeability and relative permeability of heterogeneous media, where the heterogeneity is in local permeability. We adapt this steady-state homogeneous equation approach to

a vertically integrated system in which the heterogeneity is aquifer thickness. The end result is a set of effective permeability and relative permeability functions that capture the geometric heterogeneity of a rough caprock system.

We derive the HM functions analytically for the simple cross-sectional system depicted in the inset of Figure 1 with varying top surface and flat bottom. However, in general, numerical homogenization will be necessary for realistic caprock surfaces. As with the AM approach, the objective of the homogenization is to replace the rough caprock with a flat top surface over the averaging scale of interest, resulting in an average aquifer height $\bar{H}$. This allows us to formulate the equations with only large-scale variability in the caprock surface and employ a coarser discretization. However in the HM approach, no prior assumptions are made about the permeability in the accretion layer and rock properties are homogeneous within in the averaging volume. For convenience, gravity is neglected over the averaging length scale L in the HM derivation.

Let us start with permeability upscaling. The basic approach is to posit a homogeneous equation for steady-state single-phase flow at the average scale composed of average quantities [*Renard and de Marsily*, 1997]. When the coarse scale equation is compared with the horizontal average of the fine-scale (VE) equation, the effective permeability can be inferred. This upscaling approach assumes that the heterogeneity is periodic in space and has a characteristic length scale much smaller than the total length of the domain.

To demonstrate this for our simple one-dimensional system, we have the x-component of the depth-integrated fine-scale flux $\mathbf{F}$ from Equation (7),

$$F_x = -\frac{HK}{\mu}\frac{dP}{dx} = C, \tag{26}$$

which is equal to a constant C for all x-values within L under steady-state conditions. Equation (26) can be integrated over L, and after rearrangement, results in,

$$\frac{\Delta P}{L} = -\frac{\mu C}{L}\int_0^L \frac{1}{HK}\,\mathrm{d}x, \tag{27}$$

which can be compared with the homogeneous single-phase flow equation given a pressure drop of $\Delta P/L$ across the averaging volume,

$$-\frac{\bar{H}\bar{K}}{\mu}\frac{\Delta P}{L} = C. \tag{28}$$

Combining Equations (27) and (28), we obtain the expression for horizontally upscaled permeability $\bar{K}$,

$$\frac{1}{\bar{H}\bar{K}} = \frac{1}{L}\int_0^L \frac{1}{HK}\,\mathrm{d}x. \tag{29}$$

Equation (29) indicates that the effective transmissibility ($\bar{H}\bar{K}$) for an aquifer of varying thickness is simply the harmonic average of fine-scale transmissibility over the length scale of interest.

For relative permeability, additional assumptions are required regarding the fine-scale saturation. Our approach for this step is based on the capillary equilibrium assumption [*Pickup and Stephen*, 2000; *Neuweiler and Vogel*, 2007] that is adapted to the VE rough caprock system. In the typical application of the capillary equilibrium assumption, the fine-scale capillary pressure is assumed to be at equilibrium, and therefore the coarse-scale and fine-scale capillary pressures are equivalent. This is a reasonable assumption if the applied pressure gradient is small. In this case, the saturation can be fixed at the fine-scale according to the local capillary-saturation relationship, which will be spatially varying due to heterogeneity.

In the context of a rough caprock, the fine-scale capillary pressure assumption becomes an assumption on the fine-scale CO_2-brine interface. For small pressure gradients and a horizontal averaging length much smaller than the domain, it is reasonable to assume that the ζ_M is essentially flat and $\nabla\zeta_M = 0$ in Equation (13). For a given value of ζ_M, we can fix fine-scale depth-averaged saturation S_α, equivalently we can fix h_α, which is spatially varying due to the rough caprock.

Then, following the permeability upscaling approach from above, the coarse-scale relative permeability can be determined from a series of steady-state solutions obtained at different values of ζ_M. This means that for a given value of ζ_M and the corresponding set of local saturation values S_α, the fine-scale steady-state flow equations can be integrated and set equal to a homogeneous two-phase flow equation consisting of average quantities. By repeating this process for different values of ζ_M, the coarse-scale relative permeability ($\bar{K}_\alpha$) can be calculated as a function of volume-averaged saturation ($\bar{S}_\alpha$).

For the cross-sectional system of interest, the steady state phase flux in the x-direction from Equations (7) and (9),

$$F_{\alpha x} = -\frac{HKK_\alpha}{\mu_\alpha}\frac{dP}{dx} \, .$$

which for a sharp-interface system becomes,

$$F_{bx} = -\frac{h_b K k_b^0}{\mu_b}\frac{dP}{dx} = C_b \, , \quad F_{cx} = -\frac{h_c K k_c^r}{\mu_c}\frac{dP}{dx} = C_c \, , \tag{30}$$

which are equal to constants in x at steady-state. The fine-scale phase fluxes in Equation (30) can be averaged over L,

$$\frac{\Delta P}{L} = -\frac{\mu_b C_b}{L}\int_0^L \frac{1}{h_b K k_b^0}\,\mathrm{d}x, \quad \frac{\Delta P}{L} = -\frac{\mu_c C_c}{L}\int_0^L \frac{1}{h_c K k_c^r}\,\mathrm{d}x. \tag{31}$$

and compared with the corresponding homogeneous equations for each α-phase,

$$-\frac{\bar{H}\bar{K}\bar{K}_\alpha}{\mu_\alpha}\frac{\Delta P}{L} = C_\alpha. \tag{32}$$

Then by combining Equation (31) and Equation (32) we find the following expression for coarse-scale relative permeability functions,

$$\frac{1}{\bar{H}\bar{K}\bar{K}_b} = \frac{1}{L}\int_0^L \frac{1}{h_b K k_b^0}\,\mathrm{d}x\ , \quad \frac{1}{\bar{H}\bar{K}\bar{K}_c} = \frac{1}{L}\int_0^L \frac{1}{h_c K k_c^r}\,\mathrm{d}x. \tag{33}$$

As with the upscaled permeability from Equation (29), we see that the effective relative permeability is a harmonic mean of fine-scale relative permeability values weighted by the corresponding transmissibility. This implies that if $h_c(x) = 0$ at any point x in averaging window then $\bar{K}_c = 0$, and therefore, CO_2 has zero mobility for locations of the interface equal to or higher than the local minimum of the topography. Clearly, the HM gives the same effective residual saturation for CO_2 during drainage as was found with the AM (from Equation (18)). However, an important aspect of the HM is that the shape of the CO_2 relative permeability curve will depend on the specific topography function being integrated. This is not the case for the AM which results the same relative permeability curve for different topography functions with the same trapped volume. The impact of this difference between the two effective models will be demonstrated below, where we provide a comparison for a specific caprock topography.

It should be noted that Equations (29) and (33) involve integral expressions that can be solved analytically for certain idealized systems. Alternatively, the integral can be solved numerically if necessary.

4.3. 1D application

The utility of the AM and HMs is demonstrated using a simple cross-section of an aquifer with idealized topography (Figure 4). The homogeneous aquifer has a top surface $\zeta_T(x)$ is described by a sinusoidal function

$$\zeta_T(x) = \bar{H}\left(1 + a\sin\omega x\right),$$

with scaled amplitude $a = 0.1$, wavelength $\omega = 0.01\pi$, average aquifer thickness $\bar{H} = 100$ m and a bottom boundary $\zeta_B = 0$ m. The aquifer has a 1% tilt and the coordinate system is aligned such that the vertical direction is perpendicular to the bottom boundary. The top and bottom boundaries are closed, and the side boundaries are open and fixed at hydrostatic pressure. The fluid and rock properties are given in Table 1 [*Gray et al.*, 2012].

A reference simulation was performed on the fine-scale system, such that the variation in the top surface was resolved with a relatively fine grid (number of gridblocks per wavelength $2\pi/(\omega\Delta x) = 10$). The fine-scale simulation was performed using the VE model described in Section 3 that solves the sharp-interface flow equations with a standard numerical method [*Gasda et al.*, 2011]. Migration of CO_2 after 1,000 yrs results in enhanced trapping and slower tip migration when compared with a flat caprock [*Gray et al.*, 2012].

The effective simulations employed either the AM or HM. The AM uses the effective permeability and relative permeability functions given in Equations (17) and (18), respectively, setting $H_e = 90$ m.

The HM upscales the horizontal permeability and relative permeability using the effective equations derived earlier, which can be solved analytically for a sinusoidal function. From Equation (29), we obtain effective permeability,

$$\bar{K} = K\sqrt{(1 - a^2)}. \tag{34}$$

and also relative permeabilities from Equation (33),

$$\bar{K}_c = k_c^r \frac{\sqrt{\left(\bar{h}_c/\bar{H}\right)^2 - a^2}}{\sqrt{1-a^2}}, \quad \bar{K}_b = k_b^0 \frac{\bar{h}_b}{\bar{H}}. \tag{35}$$

We observe in Equation (34) that $\bar{K}$ rescales the fine-scale permeability by a factor that decreases with increasing amplitude of the caprock. The square-root functional form implies that for values of $a \ll 1$, the scaling factor is close to unity, and $\bar{K} \approx K$. For large values of a, the vertical flow components cannot be ignored and the Dupuit assumption (vertical equilibrium) is no longer valid. When $a = 1$, then no flow occurs.

Similarly, Equation (35) reflects a reduction in CO_2 relative permeability with increasing amplitude, while the brine function is unchanged from the fine-scale function. The shape of the CO_2 relative permeability curve, shown in Figure 5, captures both the trapped volume and structure of the caprock surface.

The specific structure of the caprock topography and upscaling approach is reflected in the shape of the curve as CO_2 thickness increases beyond the trapped volume thickness. Once CO_2 becomes mobile, both curves approach the flat caprock curve ($a = 0$), but the HM relative permeability increases more rapidly because flow through the structural traps is explicitly captured in the HM upscaling approach. The non-linear shape of the HM curve also implies that the effect of topography is most important when CO_2 migrates as a relatively thin layer, i.e. at the leading edge of the plume. On the other hand, where CO_2 thickness is large relative to the height of undulations in the caprock topography, the effect of the topography on the upscaled relative permeability becomes smaller. The latter case is a reasonable result, since we expect that as CO_2 approaches fully saturated conditions, the single-phase flow equations should be recovered, which means that $\bar{K}_c$ should approach k_c^r as $\bar{h}_c$ approaches $\bar{H}$.

As shown in Figure 6, the effective simulations result in upslope plume extent and structural trapping that resemble the resolved fine-scale simulation at 1,000 yrs. In both the AM and HMs, the structurally trapped CO_2 forms a long thin layer behind the front that has a thickness equal to the amplitude of the sinusoidal function. At the leading edge of the plume, we observe a self-sharpening of the plume tip in both cases, which is caused by the effective residual saturation or zero CO_2 mobility during drainage for plume thicknesses less than the trapped volume thickness. The differences in plume location and shape of the interface between the two effective models is therefore due to differences in the relative permeability curves when CO_2 begins to flow underneath the caprock undulations.

Comparing the interface location between the AM, HM and reference simulations in Figure 7, we see that the HM result is closer overall to the reference solution than the AM. The reference simulation has an extent to 10 km, and the CO_2 is trapped almost completely up to around 8.5 km. The HM captures the tip location very well, but underestimates the volume of CO_2 in the mobile region by a small amount. This is partly because the volume of CO_2 trapped is overestimated in the effective model due to the tilt of the aquifer and can be adjusted easily to match. On the other hand, the AM significantly underestimates the plume tip location, while the center of the mobile CO_2 region lags significantly behind the reference solution.

When comparing the plume tip location across time in Figure 8, we see that initially the plume migration speed increases as determined by the curvature of the interface (the diffusive terms arising from derivatives of the ζ-terms in Equations (10) and (11)). Once the interface becomes more flat, the hyperbolic component of the equations becomes dominant and the tip speed becomes constant as predicted by Equation (25). The AM

simulation results in the slowest CO_2 migration, significantly less than the flat caprock simulation, which is expected from the analysis of shock speed in Section 4.1. The resolved simulations also results in a slower tip speed than the flat caprock case, but still migrates more quickly than the AM plume once the diffusive terms have dissipated. The HM results match quite well with the fine-grid simulations, with a slight discrepancy due to an overestimation of trapped volume as discussed above.

The reliability of both the AM and HM is clearly linked to the way in which the CO_2 relative permeability function was upscaled. We observe that both effective models capture the trapping of CO_2 in the topography behind the mobile plume quite well, which is to be expected since both models have zero relative permeability for values of CO_2 thickness less than the equivalent trapped volume thickness. However, only the HM correctly captures the migration speed of the mobile plume, which is due to averaging the fine-scale topography explicitly rather than making implicit assumptions regarding the flow behavior of CO_2 along the topography.

Given the sensitivity of CO_2 migration to fine-scale structure, we explore other functional forms of caprock roughness to gain further understanding of this effect. Two other structures were tested, triangle and square waves, and the results are summarized in Table 2. The triangle wave function is characterized by having a constant absolute value of caprock slope that changes sign periodically, while the square wave function is represented by a flat caprock with step-function changes in elevation at periodic intervals. We note that the triangle, sine and square wave functions all have the same equivalent trapped volume.

There are several interesting observations from examination of Table 2 and the accompanying Figure 9. First, despite having the same trapped volume, the triangle, sine and square wave result in different functional forms of $\bar{K}$ and $\bar{K}_c$. (The form of $\bar{K}_b$ is little effected by the top topography and brine is not trapped because the bottom boundary is flat. Therefore, we assumed the same function in all cases for simplicity.) This means that structure is important in determining the effective permeability and relative permeability functions as well as the tip speed. Thus, we can associate different structures with different degrees of caprock roughness. For instance, greater roughness leads to greater reduction in $\bar{K}$ for a given a (Figure 9a) and less curvature of $\bar{K}_c$ as a function of $\bar{h}_b$ (Figure 9b). We also note that the relative permeability curves are bounded at the top by the smooth flat surface, while the AM curve acts as a lower bound. The roughness factor will also control the theoretical late-time tip speed derived for a hyperbolic system (Equation (25)) relative to the smooth flat surface. Our results show that different degrees of roughness leads to late-time tip speeds that are between 47% and 57% times the reference speed for a smooth flat caprock (for $a = 0.1$), with square structures having a greater roughness factor than both the sinusoidal and triangular traps. We note that for this case the accretion layer model predicts a late-time tip speed that is 70% slower than reference speed. And finally, as we previously observed, the impact of structure on $\bar{K}_c$ is only significant in the region of thin CO_2 plumes ($\bar{h}_c \approx a$).

5. 2D Effective Model

The impact of heterogeneous topography 3D flow regimes is characterized by CO_2 that can flow in two lateral directions. Therefore, resistance to flow due to rugosity and roughness will lead to more complex flow behavior. For instance, if CO_2 becomes easily trapped

along the dip direction, the plume upslope speed will slow, causing more transverse spreading in the perpendicular direction. Conversely, if roughness increases in the transverse direction, then it may lead to flow focusing of the CO_2 plume and preferential upslope flow. Complexity in caprock surfaces can therefore lead to highly asymmetric footprints and more heterogeneous plume distribution.

Caprock surfaces can be upscaled by extending the one-dimensional AM and HM methods described in Section 4 to two horizontal dimensions. Although the approach is similar, the increased dimensionality introduces additional complications to the resulting effective models. First, the use of numerical homogenization is necessary to obtain a two-dimensional HM except for a few special cases. Secondly, asymmetric caprock surfaces at the fine-scale will result in anisotropic effective functions at the average scale. We determine the effective model for both symmetric and asymmetric two-dimensional caprock surfaces with the AM and HM approaches in this section.

5.1. 2D Accretion-Layer Model

In general, the AM approach in 2D involves effective permeability and relative permeability functions consisting of tensorial quantities to account for horizontal anisotropy. To start, we consider the vertical distribution of horizontal permeability,

$$\mathbf{k}(z) = \begin{cases} \mathbf{k}, & \text{if} \quad 0 \leq z < H_e \\ \mathbf{k_a}, & \text{otherwise.} \end{cases} , \tag{36}$$

where the effective aquifer height, $H_e = \bar{H}\,(1-a)$, is based on the maximum accretion layer thickness, a quantity that is independent of flow direction. We introduce the permeability quantity $\mathbf{k}_a$, which is the permeability tensor local to the maximum accretion layer. The 2D accretion layer permeability $\mathbf{k}_a$ will be equal to zero for a symmetric to-

pographical structure, but one or more components of the tensor may be non-zero for asymmetric topography. In the general case, a sub-model is required to determine the non-zero elements of $\mathbf{k}_a$ that will be specific to the caprock topography of interest.

Applying Equation (8) to Equation (36) leads to an expression for effective permeability,

$$\bar{\mathbf{K}} = \frac{H_e}{\bar{H}}\mathbf{k} + a\mathbf{k}_a, \tag{37}$$

while applying Equation (9) results in,

$$\bar{H}\bar{\mathbf{K}}_b \cdot \bar{\mathbf{K}} = \begin{cases} h_b k_b^0 \mathbf{k} & 0 \le h_b \le H_e \\ H_e k_b^0 \mathbf{k} + (h_b - H_e)\, k_b^0 \mathbf{k}_a & \text{otherwise,} \end{cases} \tag{38}$$

$$\bar{H}\bar{\mathbf{K}}_c \cdot \bar{\mathbf{K}} = \begin{cases} (H_e - h_b)\, k_c^r \mathbf{k} + a\bar{H} k_c^r \mathbf{k}_a & 0 \le h_b \le H_e \\ \left(\bar{H} - h_b\right) k_c^r \mathbf{k}_a & \text{otherwise.} \end{cases} \tag{39}$$

For symmetric surfaces where $\mathbf{k}_a = 0$, the effective equations can be simplified from the general form above.

5.2. 2D Steady-State Homogenization

Similar to the 1D homogenization in Section 4.2, effective permeability and relative permeability functions can be derived analytically for some simple function forms. For example, the effective permeability for a two-dimensional checkerboard surface, which is an extension of the square wave to two dimensions, with periodic permeability, k_1 and k_2, has been derived previously [*Obnosov*, 1996] and is equal to the geometric mean of the two permeability values. Translating this result to a rough caprock surface with alternating elevation values $\bar{H}(1+a)$ and $\bar{H}(1-a)$ results in the following isotropic tensorial expression for effective permeability

$$\bar{\mathbf{K}} = \mathbf{K}\sqrt{(1 - a^2)} \tag{40}$$

which is interestingly a similar expression that of the 1D sine wave function derived previously. The HM effective relative permeability functions for the checkerboard surface

612 are also the two-dimensional form of the expressions derived for the sine wave function
613 (Equation (35)).

614 For a caprock surface consisting of geometrical inclusions (cubic, spherical and elliptical)
615 with a horizontal dimension much smaller than the spacing between the structures, the
616 effective permeability and relative permeability functions can also be found analytically.
617 However, since we are ultimately interested in realistic caprock surfaces, we refer the
618 reader to the literature for more details on these analytical solutions [*Andrianov et al.*,
619 1999; *Renard and de Marsily*, 1997].

620 For more complex topographical surfaces, numerical homogenization is necessary for the
621 HM approach. To do this, steady-state upscaling simulations are performed on different
622 3D systems, resolving the fine-scale structure with the VE model described in Section 3.
623 Periodic pressure boundary conditions are applied with a small pressure gradient in the
624 horizontal direction. For asymmetric surfaces, the simulation must be performed in both
625 horizontal directions.

626 Effective permeability is calculated by substitution of the resulting horizontal flux into
627 the upscaled equation (Equation (28)) and solving for $\bar{\mathbf{K}}$. For relative permeability cal-
628 culations, a capillary equilibrium assumption is applied, which means a stationary CO_2
629 interface is fixed while the flow simulations are performed. The resulting horizontal CO_2
630 flux, along with other known quantities, is then used to determine the upscaled relative
631 permeability using Equation (32).

5.3. 2D Application

632 The first caprock structure is a symmetric sinusoidal surface described by,

$$\zeta_T(x, y) = \bar{H}\left[1 + \alpha_1\left(\sin\omega_1 x + \sin\omega_1 y\right)\right],$$

633

and the second is an asymmetrical system of staggered elliptical structures, with the top surface given by

$$\zeta_T(x,y) = \bar{H}\left(1 + \alpha_2 e^{-\gamma}\right),$$

where

$$\gamma = \sin^2 \omega_2(x-y) + \sin^2 \omega_2(x+y) + 2\sin^2 2\omega_2 x.$$

In the above equations $\alpha_1 = 0.1$, $\alpha_2 = 0.25$, and ω_1 and ω_2 are set to obtain an even number of periods in the domain. The sinusoidal surface is symmetric in x and y, while the elliptical structure is asymmetric (Figure 10).

To derive the AM equations, the maximum trapped volume is $a = 0.04$ in both cases. The submodel for the accretion layer permeability $\mathbf{k}_a$ can be obtained from the geometry. For the sinusoidal surface, symmetry results in $\mathbf{k}_a = 0$. The elliptical surface is anisotropic, therefore $\mathbf{k}_a$ has diagonal components $k_{a,xx} = 0$ and $k_{a,yy} = 0.375K$. Here, the y-direction is parallel to the long dimension of the elliptical structures and perpendicular to the dip direction. There are no off-diagonal components because the coordinate system is aligned with the principal flow direction. For the HM method, we apply numerical homogenization to the caprock surfaces, which become piece-wise linear functions in the VE model. For both systems the bottom is flat at $\zeta_B = 0$ and the coordinate system is aligned with the principal direction of flow.

We observe the CO_2 relative permeability functions are a function of the upscaling approach and the fine-scale structure of the surface (Figure 11). For the HM-derived functions, the symmetrical sinusoidal surface leads to an isotropic relative permeability, while the orientation of the elliptical structures leads to anisotropy in the x and y diagonal components of the upscaled tensor. This anisotropy implies that CO_2 flow at a given

relative permeability requires a greater thickness in the x-direction than the y-direction, which is clear from the anisotropic trapped volume tensor $\mathbf{a}$ for this caprock surface. We also observe that the sinusoidal caprock results in a nearly linear relative permeability function, whereas the curves for the elliptical structures are less linear and reach the flat caprock (zero roughness) curve more quickly. As in the cross-sectional case, the AM acts as a lower bound on CO_2 relative permeability. We note that the difference between the AM and HM curves for the sinusoidal surface is negligible until the CO_2 plume thickness becomes larger than 20% of the average formation thickness.

Resolved and effective simulations were performed for systems with the caprock surfaces (either sinusoidal or elliptical) as the top boundary of aquifers extending 10 km in both lateral directions and average thickness of 100 m. In each simulation, all lateral boundaries are closed except for the upper boundary at $x = 10$ km which is assigned a fixed pressure condition. The fluid and rock properties are the same as for the one-dimensional simulations presented above. The initial condition is a 2-km length square of fully saturated CO_2 centered at $(x, y) = (2, 5)$ km.

The resolved simulations for these 2D systems (Figure 12), results in a spatial distribution of mobile CO_2 that reveals the fine-scale structure of the topography. The sinusoidal surface is slightly elongated in the dip direction, while the elliptical surface is wider in the cross-dip direction than along the dip axis. In each case, we observe structurally trapped CO_2 downslope in local maxima where CO_2 has become disconnected from the rest of the mobile plume. Residual CO_2, when added to the mobile CO_2 thickness, gives the maximum thickness of CO_2 at any given location in the domain. Besides the location

around the initial condition, the residual thickness is quite small, which implies that CO_2 is migrating as a very thin layer, filling up structural traps as it travels updip.

The HM and AM effective simulations, which use the upscaled relative permeability curves from Figure 11, produce average CO_2 thickness in each grid cell which is then downscaled to obtain the fine-scale variation in thickness due to subscale topography. This allows for a more direct comparison with the resolved simulations in Figure 12. The downscaled HM and AM results for the sinusoidal give a good comparison with the resolved simulations for mobile and residual CO_2 after 300 years. The outer edge of the plume corresponds well with the resolved simulations in both cases. For the elliptical surface, the HM model compares well with the resolved simulation in both the shape of the plume footprint and updip migration. There is some slight underestimation of lateral (cross-dip) plume spreading. The AM results show a large discrepancy with the resolved case, greatly underestimating the updip plume migration after 300 years.

The comparison of maximum upslope extent (Figure 13) shows that both HM and AM effective simulations agree reasonably well with the resolved sinusoidal simulation, while only the HM simulation compares closely with the resolved elliptical simulation. For the resolved simulations, the impact of fine-scale structure leads to a slower CO_2 migration for the sinusoidal surface than the elliptical surface (as indicated in the upscaled CO_2 relative permeability function). The HM simulations reproduce this difference quite well, with some discrepancy in the exact plume location over time. For instance, the HM slightly underpredicts the sinusoidal plume location while overpredicting for the elliptical surface. Some of the difference may be attributed to insufficient resolution of the fine-scale topography in the resolved simulations. There also may be some influence of the

boundary condition as the plume approaches the upper boundary. Despite these minor issues, the HM simulations give a good approximation of the plume migration due to caprock roughness. The AM simulation gives essentially the same plume migration for both sinusoidal and elliptical surface because the CO_2 relative permeability along the dominant direction of flow ($\bar{K}_{n,xx}$) is the same for both cases. The AM replicates the sinusoidal case quite well because the HM and AM curves are the same in the region of small CO_2 thickness.

6. Discussion and Conclusions

Caprock topography may be an important factor affecting long-term CO_2 migration in subsurface storage formations. Small-scale geometric heterogeneity and surface roughness can reduce the plume footprint and maximum extent as well as trap CO_2 in subscale structural feature. Many modeling studies assume a smooth caprock, potentially overestimating upslope migration speeds for systems where caprock roughness provides additional storage of CO_2 in the dip direction. However, in some special cases, rugosity may lead to preferential flow and faster upslope migration speed than predicted by a smooth caprock. Therefore, it is important to be able to model the migration of CO_2 plumes over large distances in structurally heterogeneous systems.

Vertical equilibrium methods are an attractive option because of their reliability and efficiency when applied to storage formations with caprock topography that can be resolved by seismic observations. However, some horizontal upscaling of the flow equations is required to capture caprock roughness below seismic resolution. In this paper, we derived effective equations using two approaches, AM and HM, and compared the reliability

of the upscaled equations with a fine-scale model. Our results show the effective modeling approach has potential to simplify geological models for CO_2 sequestration.

The effective model consists of horizontally upscaled permeability and relative permeability VE functions that capture the impact of a spatially varying top boundary (i.e. a rough caprock). These upscaled functions are used in place of the usual depth-averaged functions that appear in the VE model whenever subscale topography is present. We examined two approaches to upscaling, where both employ the VE assumptions of gravity segregation and vertical equilibrium. The first (AM) assumes the existence of an accretion layer with a volume equivalent to the trapped volume created by the topography. This layer is assumed to have zero horizontal permeability before the equations are vertically integrated. The second approach (HM) uses steady-state homogenization to upscale the VE equations directly across a chosen horizontal length scale. For upscaling two-phase flow with this approach, a static capillary equilibrium assumption is applied, which requires a stationary interface between CO_2 and brine across the averaging scale. This is the VE version of the capillary limit of traditional flow-based relative permeability upscaling.

We applied the AM and HM approach to several 2D and 3D systems with different functional forms of caprock roughness. The AM equations can be derived analytically by piecewise integration. For the HM approach, the VE equations can be homogenized analytically for cross-sectional (2D) systems, resulting in upscaled constitutive equations that are simply the harmonic average of the fine-scale function (permeability or relative permeability) weighted by formation height. The caprock surfaces of the 3D systems must be homogenized numerically except for a few special cases. We observed several important features of the resulting AM and HM effective functions. First, in all cases

caprock roughness leads to a reduction in effective permeability in proportion to the trapped volume, while CO_2 relative permeability is reduced significantly especially for thin CO_2 plumes. Additionally, upscaling the fine-scale process of CO_2 spilling into subscale structural traps as it migrates updip results in an effective residual CO_2 saturation during the drainage process. And finally, the HM functions vary in curvature according to the roughness of each topography, while the AM function is the same for all structures since it is based only on the equivalent trapped volume and does not consider fine-scale structure explicitly. As a result, the AM effective relative permeability functions are always linear with respect to CO_2 plume thickness and represent the lower bound on the reduction in permeability and relative permeability due to caprock roughness in all cases examined here.

The AM and HM effective equations were implemented into the VE framework and compared with fine-scale VE simulations of the 2D and 3D systems. We found that in all cases the HM model correctly captured the impact of topography on plume footprint and upslope migration speed in 2D and 3D systems. On the other hand, the AM could only reproduce the fine-scale solution for very rough caprocks, which are cases where the linear AM effective functions closely match the upscaled functions derived from the HM approach. It should be noted that although the AM method was not as effective as the HM in the computational experiments, the accretion-layer concept allows for analytical solutions that give good insight into the behavior of the equations for rough caprock systems.

Because the HM approach leads to a more reliable upscaled model, the implication of this work is that horizontal upscaling requires some detailed knowledge of the fine-scale

structure beyond just a measure of trapped volume. The HM effective equations can be used to identify the important parameters of geologic model required for developing a reliable effective model. These parameters may include several features of structural traps, such as change of surface slope within a structural trap, the distance between traps, or the orientation of the structures relative to the large-scale dipping plane of the storage formation. An evaluation of the geologic model parameter space will be the subject of future work.

This papers demonstrates the ability of an effective model to capture CO_2 migration in the presence of fine-scale variation in caprock topography. With this modeling approach, the geology can be simplified in computational studies of CO_2 migration in structurally heterogeneous systems. This reduces the need for expensive grid refinement, a distinct advantage given the large spatial and temporal domains of CO_2 sequestration. More efficient simulation of CO_2 migration and trapping gives greater flexibility in exploring the geological parameter space of CO_2 storage formations. In addition, the effective model allows for coupling with more complex geomechanical or geochemical models without the need to resolve detailed geological features. Thus, the resulting combined knowledge from upscaled and fine-scale models can aid in our understanding of CO_2 migration in complex systems. Ultimately, the development of simplified modeling tools such as this one will be required for evaluating and mitigating risk of long-term geological CO_2 storage operations.

Acknowledgments. This work was supported in part by the MatMoRA project (Mathematical Modelling and Risk Assessment of CO_2 storage), financed by the Research

790 Council of Norway and Statoil. Partial funding was also provided by U.S. National Science

791 Foundation grant ATM-0941235 and U. S. Department of Energy grant DE-SC0002163.

References

Alberta Geological Survey, Geological maps. http://www.ags.gov.ab.ca, 2011.

Ambrose, W. A., S. Lakshminarasimhan, M. H. Holtz, V. Nunez-Lopez, S. D. Hovorka, and I. Duncan, Geologic factors controlling CO_2 storage capacity and permanence: case studies based on experience with heterogeneity in oil and gas reservoirs applied to CO_2 storage, *Environmental Geology*, *54*(8), 1619–1633, 2008.

Andrianov, I. V., G. A. Starushenko, V. V. Danishevs'kyy, and S. Tokarzewski, Homogenization procedure and pade approximants for effective heat conductivity of composite materials with cylindrical inclusions having square cross-section, *Proceedings: Mathematical, Physical and Engineering Sciences*, *455*(1989), 3401–3413, 1999.

Bear, J., *Dynamics of Fluids in Porous Media*, American Elsevier Publication Co., New York, N.Y., 1972.

Bellian, J., C. Kerans, and D. Jennette, Digital outcrop models: Applications of terrestrial scanning lidar technology in stratigraphic modeling, *Journal of Sedimentary Research*, *75*(2), 166–176, 2005.

Celia, M. A., and J. M. Nordbotten, Practical modeling approaches for geological storage of carbon dioxide, *Ground Water*, *47*(5), 627–638, 2009.

Coats, K., J. Dempsey, and J. Henderson, Use of vertical equilibrium in 2-dimensional simulation of 3-dimensional reservoir performance, *SPE J.*, *11*(1), 63–71, 1971.

Dietz, D. L., A theoretical approach to the problem of encroaching and by-passing edge water, in *Proceedings of Akademie van Wetenschappen*, vol. 56-B, p. 83, 1953.

Gasda, S. E., J. M. Nordbotten, and M. A. Celia, Vertical equilibrium with sub-scale analytical methods for geological CO_2 sequestration, *Computational Geosciences*, *13*(4),

469–481, 2009.

Gasda, S. E., J. M. Nordbotten, and M. A. Celia, Vertically-averaged approaches for CO_2 injection with solubility trapping, *Water Resources Research*, *47*, W05,528, 2011.

Gasda, S. E., J. M. Nordbotten, and M. A. Celia, Application of simplified models to CO_2 migration and immobilization in large-scale geological systems, *International Journal of Greenhouse Gas Control*, *9*, 72–84, 2012.

Gray, W. G., P. Herrera, S. E. Gasda, and H. K. Dahle, Derivation of vertical equilibrium models for CO_2 migration from pore scale equations, *International Journal of Numerical Analysis and Modeling*, *9*(3), 745–776, 2012.

Hermanrud, C., et al., Storage of CO_2 in saline aquifers-lessons learned from 10 years of injection into the Utsira Formation in the Sleipner area, *Energy Procedia*, *1*(1), 1997–2004, 2009.

Hesse, M. A., F. M. Orr, and H. A. Tchelepi, Gravity currents with residual trapping, *Journal of Fluid Mechanics*, *611*, 35–60, 2008.

Huppert, H., and A. Woods, Gravity-driven flows in porous layers, *J. Fluid Mech.*, *292*, 55–69, 1995.

Ingeborg, L., and H. Nilsen, Numerical aspects of using vertical equilibrium models for simulating CO_2 sequestration, in *Proceedings of 12th European Conference on the Mathematics of Oil Recovery : ECMOR XII, 6-9 September 2010, Oxford, UK.*, 2010.

Jackson, C. A.-L., H. Grunhagen, J. A. Howell, A. L. Larsen, A. Andersson, F. Boen, and A. Groth, 3d seismic imaging of lower delta-plain beach ridges: lower Brent Group, northern North Sea, *Journal of the Geological Society*, *167*, 1225–1236, 2010.

Jones, R. R., K. J. W. McCaffrey, P. Clegg, R. W. Wilson, N. S. Holliman, R. E. Holdsworth, J. Imber, and S. Waggott, Integration of regional to outcrop digital data: 3D visualisation of multi-scale geological models, *Computers & Geosciences*, *35*(1), 4–18, 2009.

Juanes, R., C. W. MacMinn, and M. L. Szulczewski, The footprint of the CO_2 plume during carbon dioxide storage in saline aquifers: Storage efficiency for capillary trapping at the basin scale, *Transport in porous media*, *82*(1), 19–30, 2010.

Lake, L., *Enhanced Oil Recovery*, Englewood Cliffs, 1989.

Leveque, R., *Numerical Methods for Conservation Laws*, Birkhåuser Verlag, 1990.

MacMinn, C. W., M. Szulczewski, and R. Juanes, CO_2 migration in saline aquifers. Part 1. Capillary trapping under slope and groundwater flow, *Journal of Fluid Mechanics*, *662*, 329–351, 2010.

Neufeld, J. A., and H. E. Huppert, Modelling carbon dioxide sequestration in layered strata, *J. Fluid Mech.*, *625*, 353–370, 2009.

Neuweiler, I., and H.-J. Vogel, Upscaling for unsaturated flow for non-Gaussian heterogeneous porous media, *Water Resources Research*, *43*(3), W03,443, doi: 10.1029/2005WR004771, 2007.

Nilsen, H., P. Herrera, M. Iding, C. Hermanrud, J. Nordbotten, K. Lie, and H. Dahle, Field-case simulation of CO_2-plume migration using vertical-equilibrium models., in *Proceedings of 10th International Conference on Greenhouse Gas Control Technologies, Amsterdam, The Netherlands.*, 2010.

Nilsen, H., A. R. Syversveen, K.-A. Lie, J. Tveranger, and J. M. Nordbotten, Impact of top-surface morphology on CO_2 storage capacity, *International Journal of Greenhouse*

Gas Control, under review, 2012.

Nordbotten, J. M., and M. A. Celia, Similarity solutions for fluid injection into confined aquifers, *J. Fluid Mech.*, *561*, 307–327, 2006.

Nordbotten, J. M., and M. A. Celia, *Geological Storage of CO_2: Modeling Approaches for Large-Scale Simulation*, John Wiley & Sons, Inc., 2012.

Nordbotten, J. M., and H. K. Dahle, Impact of the capillary fringe in vertically integrated models for CO_2 storage, *Water Resources Research*, *47*, W02,537, 2011.

Obnosov, Y. V., Exact solution of a boundary-value problem for a rectangular checkerboard field, *Proceedings of The Royal Society of London Series A: Mathematical, Physical and Engineering Sciences*, *452*(1954), 2423–2442, 1996.

Pickup, G., and K. Stephen, An assessment of steady-state scale-up for small-scale geological models, *Petroleum Geoscience*, *6*(3), 203–210, 2000.

Pringle, J. K., R. L. Brunt, D. M. Hodgson, and S. S. Flint, Capturing stratigraphic and sedimentological complexity from submarine channel complex outcrops to digital 3D models, Karoo Basin, South Africa, *Petroleum Geoscience*, *16*(4), 307–330, 2010.

Renard, P., and G. de Marsily, Calculating equivalent permeability: a review, *Advances in Water Resources*, *20*(5–6), 253–278, 1997.

Yortsos, Y. C., A theoretical analysis of vertical flow equilibrium, *Transport in Porous Media*, *18*(2), 107–129, 1995.

Table 1. Parameters used in all simulations.

Parameter	**Symbol**	**Value**	**Unit**
CO_2 density	ρ_c	696	kg/m^3
Brine density	ρ_b	1000	kg/m^3
CO_2 viscosity	μ_c	$5 \cdot 10^{-5}$	Pa·s
Brine viscosity	μ_b	$3 \cdot 10^{-4}$	Pa·s
CO_2 residual saturation	s_{cr}	0.0947	-
Brine residual saturation	s_{br}	0.1970	-
Porosity	ϕ	0.2	-
Permeability (homogeneous & isotropic)	K	100	mD
Aquifer slope	θ	0.57 (=1.0)	$\circ$ (%)

Table 2. Summary of effective permeability and relative permeability functions (HM) and tip speed for different functional forms of caprock topography, where $\hat{h}_b = \bar{h}_b/\bar{H}$ and $\hat{h}_b \leq a$).

Topography	$\bar{K}$	$\bar{K}_b$	$\bar{K}_c$	v_c^*/v_0 $(a = 0.1)$
flat	K	$k_b^0 \hat{h}_b$	$k_c^r \left(1 - \hat{h}_b\right)$	1.0
triangle	$2aK \left[\ln\left(\frac{1+a}{1-a}\right)\right]^{-1}$	$k_b^0 \hat{h}_b$	$\frac{k_c^r \ln\left((1+a)/(1-a)\right)}{\ln\left((1-\hat{h}_b+a)/(1-\hat{h}_b-a)\right)}$	0.57
sine	$K\sqrt{(1-a^2)}$	$k_b^0 \hat{h}_b$	$k_c^r \frac{\sqrt{\left(1-\hat{h}_b\right)^2 - a^2}}{\sqrt{(1-a^2)}}$	0.53
square	$K\left(1-a^2\right)$	$k_b^0 \hat{h}_b$	$k_c^r \frac{\left(1-\hat{h}_b\right)^2 - a^2}{\left(1-\hat{h}_b\right)\left(1-a^2\right)}$	0.47

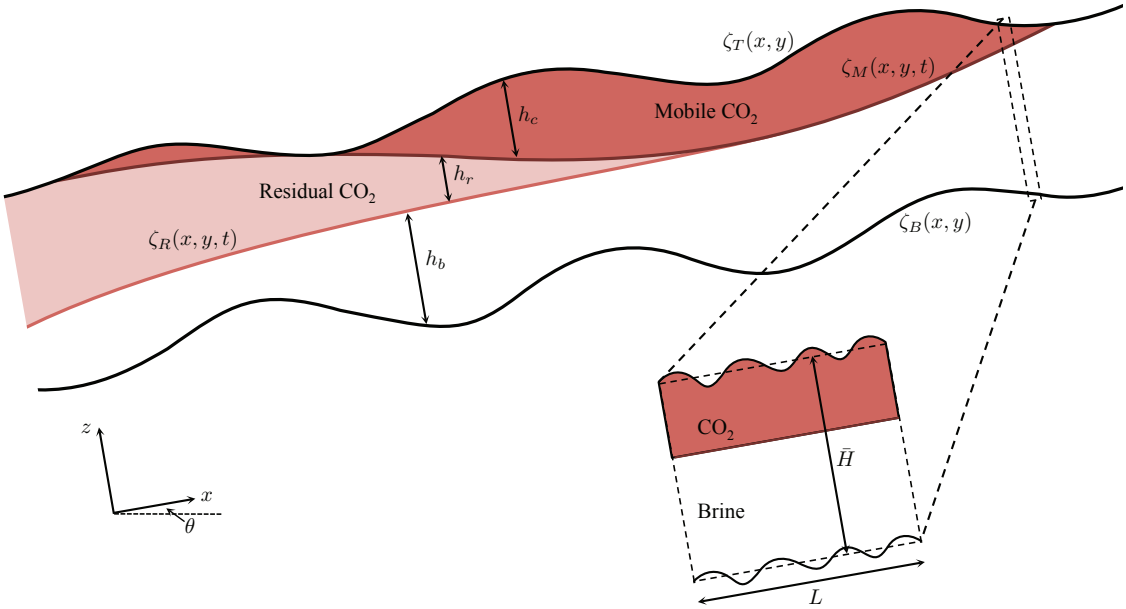

Figure 1. Schematic of CO_2 migration and residual trapping in an aquifer with varying caprock topography. Inset shows the rough caprock topography below the scale of resolution that is upscaled over an averaging length L.

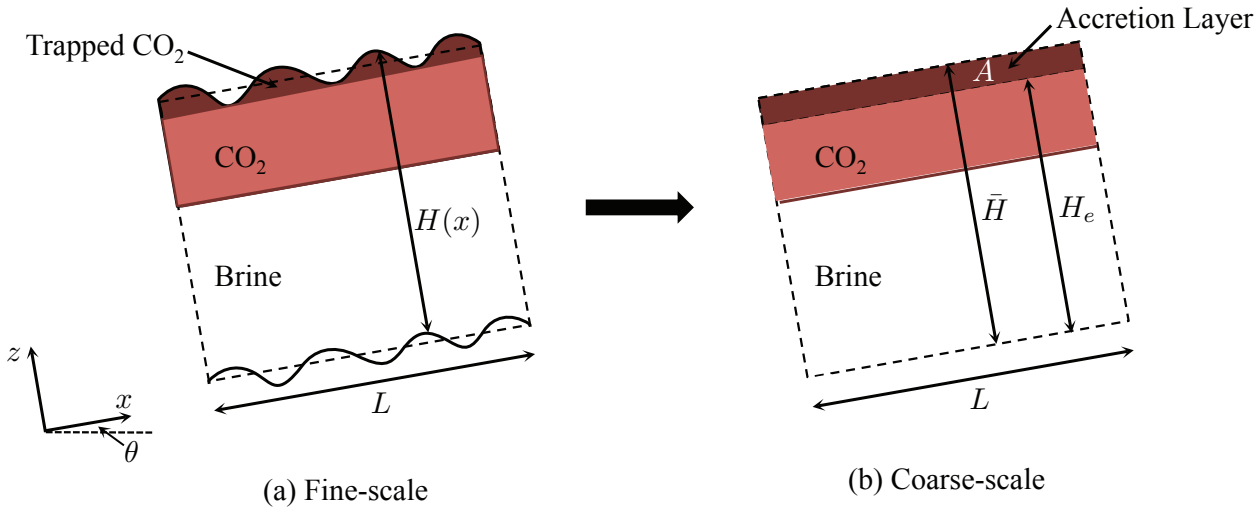

Figure 2. Schematic of fine-scale varying caprock topography system (a) that is upscaled with the AM approach to (b) using an accretion layer of zero horizontal permeability.

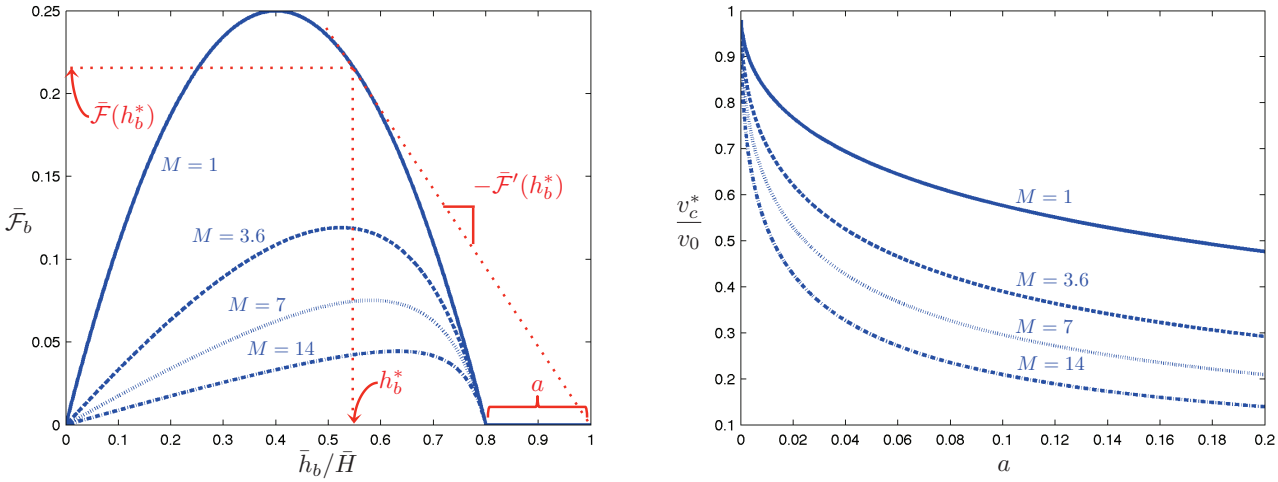

Figure 3. Example of the AM flux function, $\bar{\mathcal{F}}_b$ (left), needed to determine the shock speed v_c^* (right) as a function of scaled amplitude of caprock topography, $a = A/\bar{H}$, and the mobility ratio M.

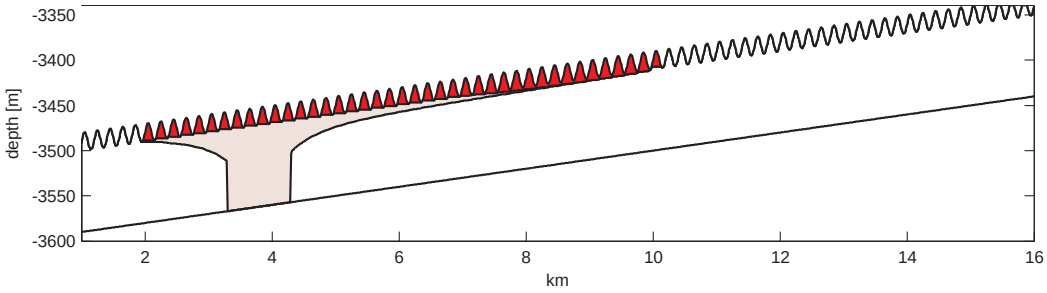

Figure 4. Reference model results for CO_2 phase thickness (dark) and CO_2 residual trapping (light) in an aquifer cross-section with the top surface given by a sinusoidal surface, $\zeta_T(x) = \bar{H}(1 + a\sin\omega x)$, where $\bar{H} = 100$ m, $L = 20$ km, $a = A/\bar{H} = 0.1$, and the wavelength $\omega = 0.01\pi$.

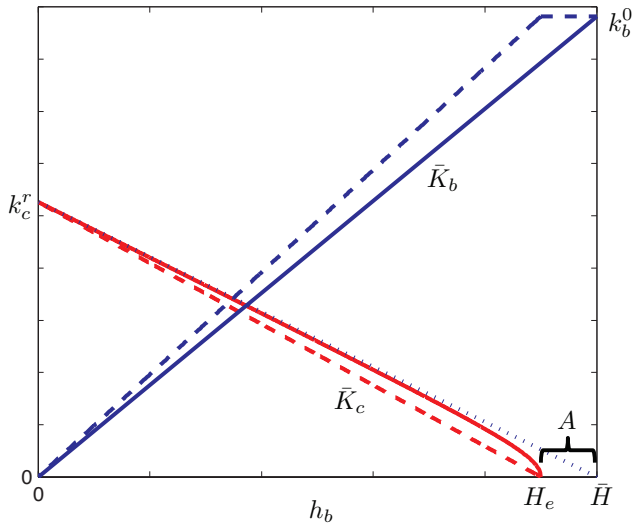

Figure 5. Upscaled relative permeability for a system the caprock surface $\zeta_T(x) = \bar{H}\,(1 + a \sin x)$ for the HM (solid lines). Effective functions obtained from the AM are shown for comparison (dashed lines).

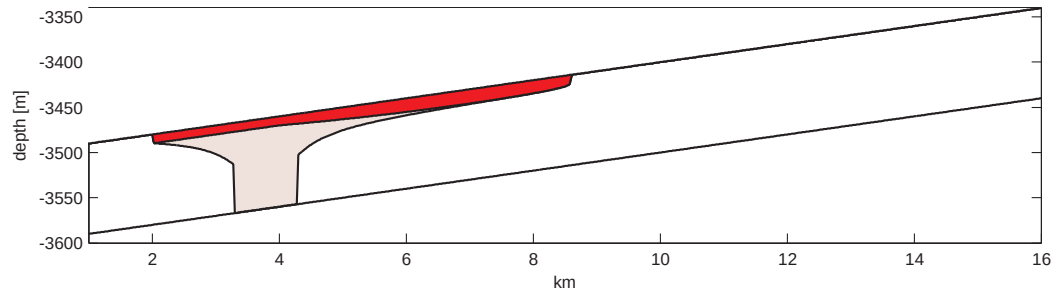

(a) AM

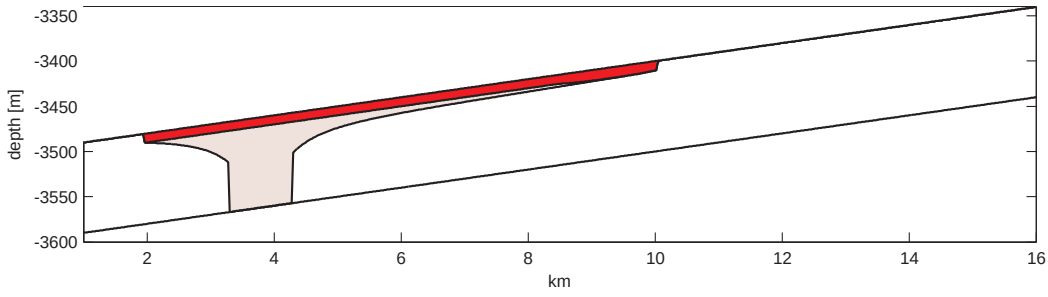

(b) HM

Figure 6. Effective model results for non-wetting phase thickness (dark) and residual trapping (light) in an aquifer cross-section with a flat top and horizontally upscaled relative permeability.

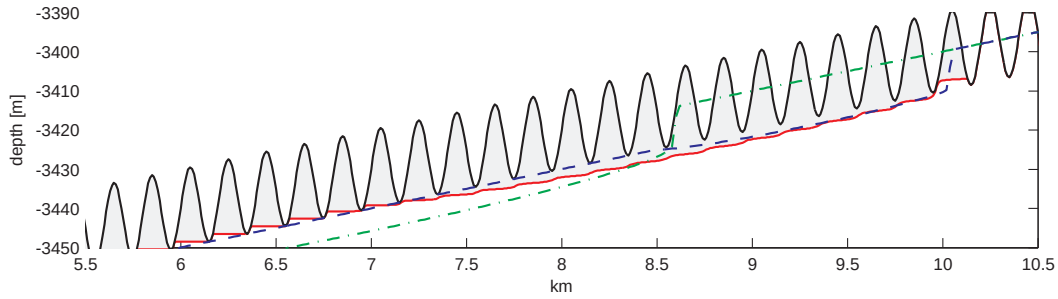

Figure 7. Comparison of reference (red-outline) and effective model results (AM–dash-dotted green; HM–dashed blue) for CO_2 interface location at 1000 yrs, $a = 0.1$.

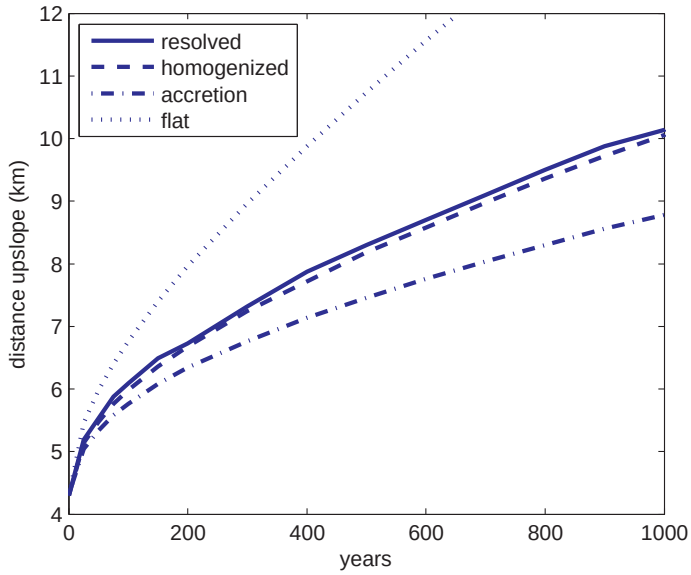

Figure 8. Maximum upslope extent of CO_2 over time in an aquifer with caprock described by $\zeta_T(x) = \bar{H}(1 + a\sin(\omega x))$, with $a = 0.1$. Shown are results from the reference (solid) and effective simulations using the AM (dash-dotted) and HM (dashed). Also shown is CO_2 migration in a system with a flat caprock, or $a = 0$ (dotted).

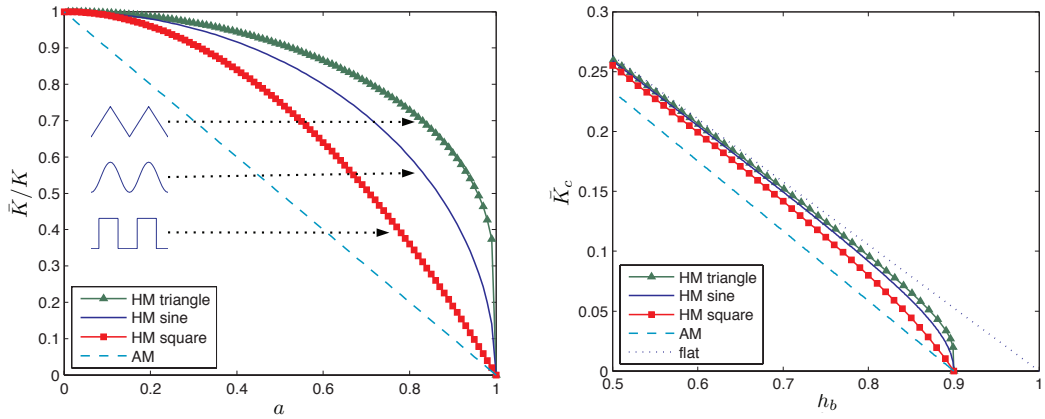

Figure 9. Effective model functions for different caprock topographies listed in Table 2: triangle, sine, and square wave. The effective permeability scaling factor (left) is plotted as a function of $a = A/\bar{H}$. Effective CO_2 relative permeability functions (right) from the HM formulation are compared with the AM function for the same equivalent trapped volume and a flat caprock with no roughness. Note the plot scale focuses on larger values of $\bar{h}_b$.

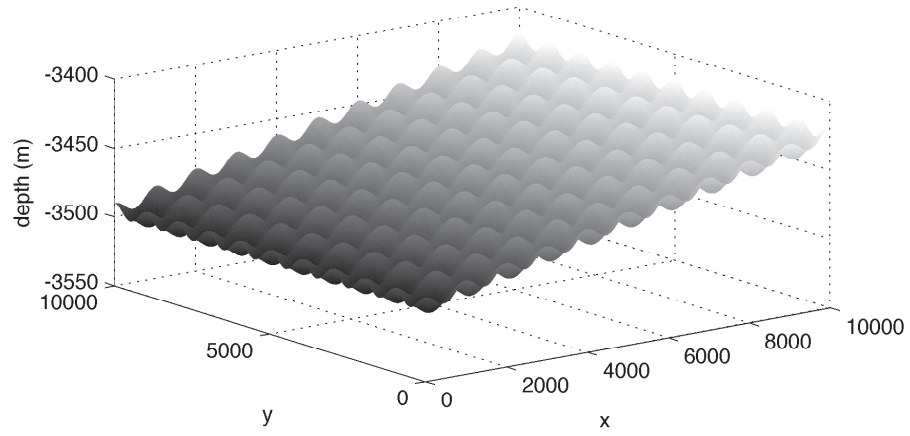

(a) sinusoidal

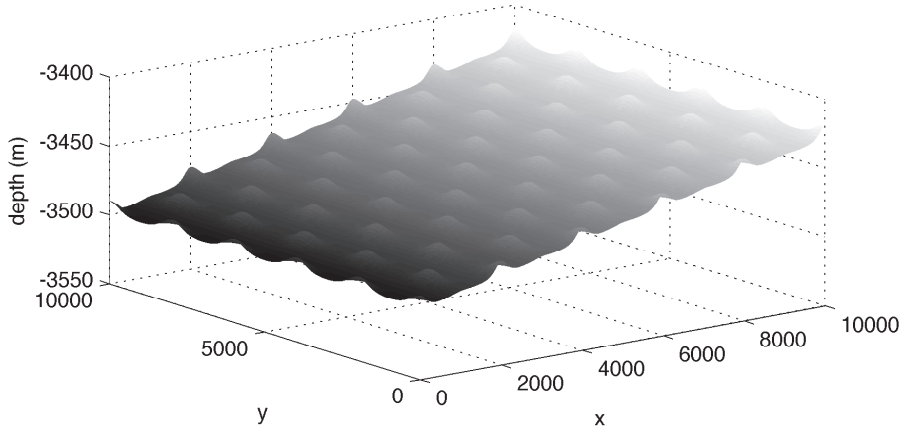

(b) elliptical

Figure 10. Fine-scale model of caprock surfaces, (a) sinusoidal and (b) elliptical, which are upscaled in the AM and HM effective model application.

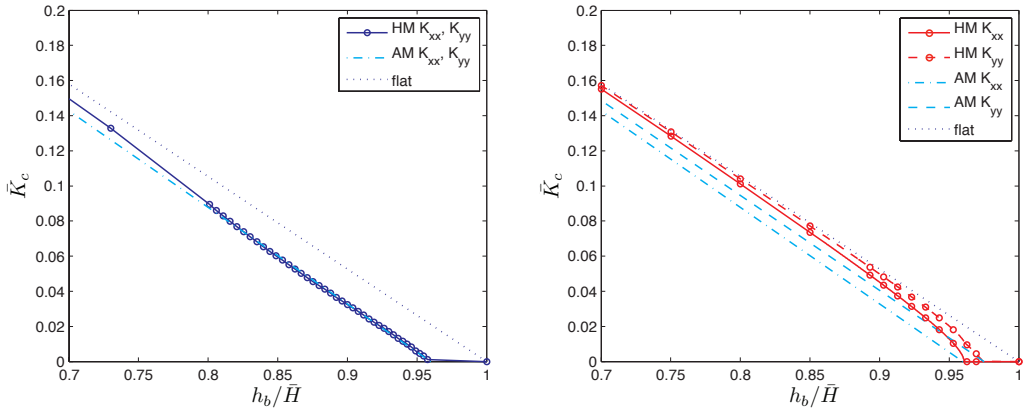

Figure 11. Effective CO_2 relative permeability for caprock surfaces having either a sinusoidal (left) or elliptical (right) structure derived using both the AM and HM effective equations. Note the plot scale focuses on larger values of $\bar{h}_b$.

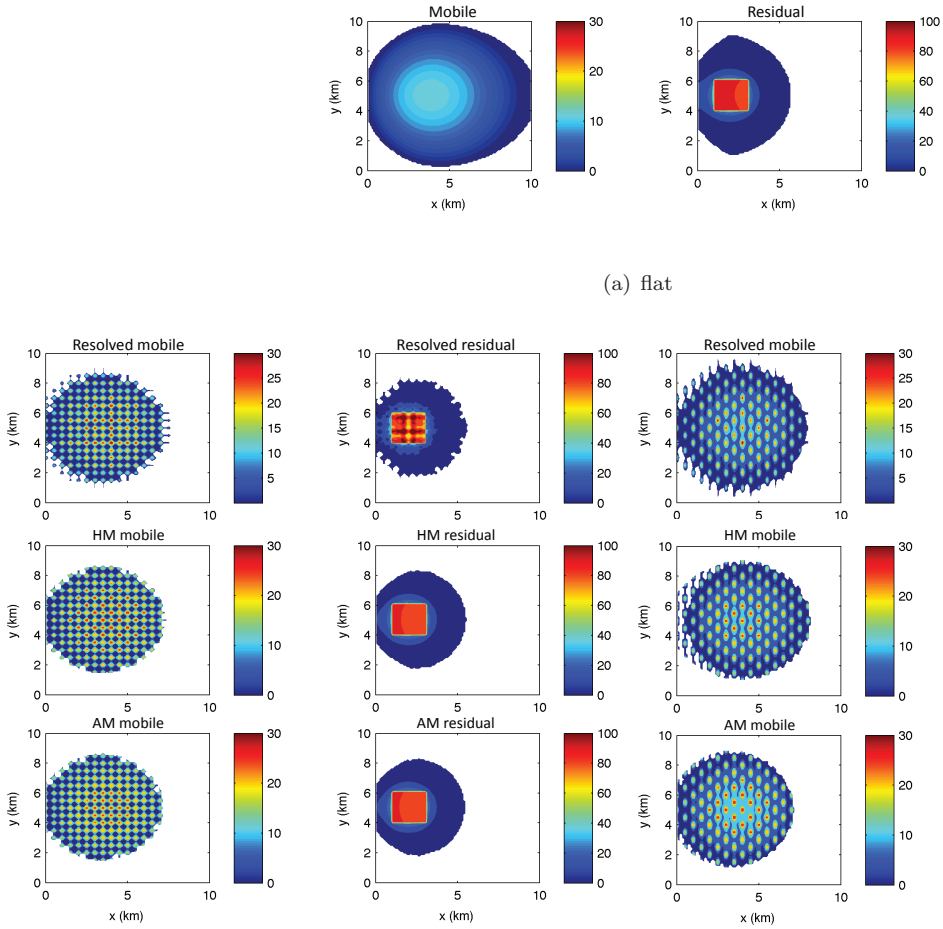

(a) flat

(b) sinusoidal

(c) elliptical

Figure 12. Spatial distribution at 300 yrs of mobile and residual CO_2 (thickness in meters) for resolved and effective simulations of caprock surfaces having a structure that is flat (a), sinusoidal (b) or elliptical (c). The HM and AM effective CO_2 thicknesses have been downscaled to the resolution of fine-scale topography. The formation dip is in the x-direction.

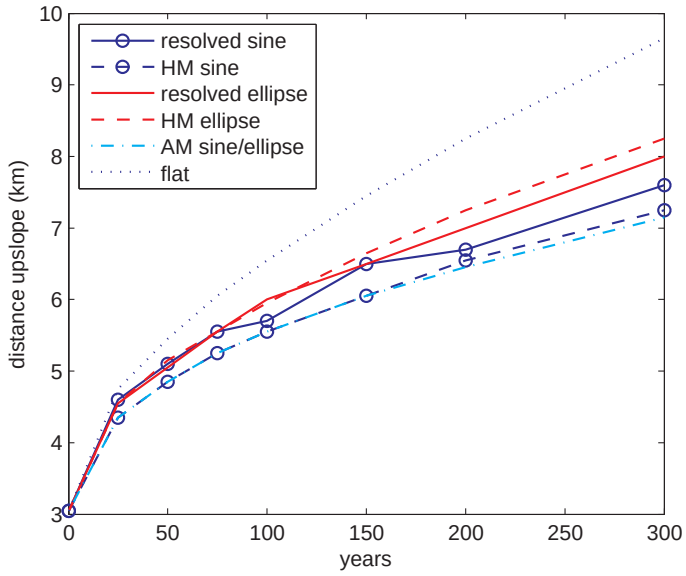

Figure 13. Maximum upslope extent of CO_2 for resolved and effective simulations of caprock surfaces having either a sinusoidal or elliptical structure.